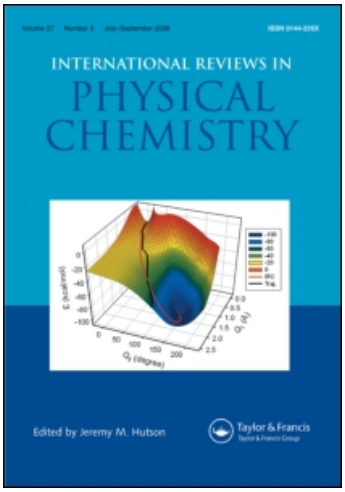

International Reviews in Physical Chemistry
Publication details, including instructions for authors and subscription information:
http://www.informaworld.com/smpp/title~content=t713724383

Structural studies on catalysts and solid surfaces

Haruo Kuroda[a]; Yasuhiro Iwasawa[a]
[a] Department of Chemistry, Faculty of Science, The University of Tokyo, Tokyo, Japan

To cite this Article Kuroda, Haruo and Iwasawa, Yasuhiro(1989) 'Structural studies on catalysts and solid surfaces', International Reviews in Physical Chemistry, 8: 2, 207 — 234
To link to this Article: DOI: 10.1080/01442358909353229
URL: http://dx.doi.org/10.1080/01442358909353229

INTERNATIONAL REVIEWS IN PHYSICAL CHEMISTRY, 1989, VOL. 8, NOS. 2/3, 207–234

Structural studies on catalysts and solid surfaces

By HARUO KURODA and YASUHIRO IWASAWA
Department of Chemistry, Faculty of Science, the University of Tokyo,
Hongo, Bunkyo-ku, Tokyo 113, Japan

Studies concerning the structures of heterogeneous catalysts and those of adsorbed layers on solid surfaces have rapidly progressed in the last ten years due to the development of a variety of new experimental techniques, including extended X-ray absorption fine structure (EXAFS) spectroscopy. This paper gives a brief review of the experimental facilities in Japan for EXAFS and surface EXAFS (SEXAFS) spectroscopy by use of synchrotron radiation, EXAFS studies on catalysts and in particular those related to the structural changes of catalysts during catalytic reactions, the soft X-ray standing wave (SW) method, structural studies on sulphur adsorption on nickel crystal surfaces by means of SEXAFS and the SW method, and some recent work on the structures of adsorbed layers by other experimental techniques.

1. Introduction

The structures of solid surfaces are usually considerably different from those in the bulk solid state. For many decades, there were only very limited techniques to investigate the structures of solid surfaces, so that most studies were of the phenomenological type that did not give detailed information on the real surface structure. In the cases of heterogeneous catalysts, there were almost no experimental methods to obtain direct structural information, hence the structures of catalysts remained unclear although extensive investigations had been carried out on catalysis. A dramatic change has recently taken place in the field of surface science. Namely, the development of ultra-high vacuum technology has made it possible to investigate the properties of well defined single-crystal surfaces, and at the same time a variety of new techniques have been developed for the characterization of solid surfaces. These situations are producing rapid and remarkable progress in surface science.

Several research projects on solid surfaces involving both physicists and chemists have been carried out in Japan during these ten years. Among them there was the one entitled 'Dynamical Processes in Solid Surface', which was sponsored in the period 1981–1984 by the Specific Research Grant-in-Aid for Scientific Research of the Ministry of Education, Science and Culture. This had a large effect on the research activities in the physical chemistry of solid surfaces. The research work carried out in this project has been published in the report 'Dynamical Processes in Solid Surface' edited by K. Tamaru (1985). Most of the work reviewed in this paper is directly or indirectly related to this research project.

Among the new techniques of surface characterization, extended X-ray absorption fine structure (EXAFS) spectroscopy is of great importance for structural studies of heterogeneous catalysts. EXAFS spectroscopy has made it possible for the first time to determine the bonding states of metal atoms in supported metal catalysts. It allows us to investigate the structural changes occurring in the process of catalysis. This has opened new possibilities for the study of catalysis.

0144-235X/89 $3·00

EXAFS spectroscopy can be applied also to the structural study of an adsorbed layer formed on a single-crystal surface. One can obtain the spectrum corresponding to the X-ray absorption spectrum of the chemical species adsorbed on a single-crystal surface by employing a surface-sensitive detection method such as the measurement of the intensity of Auger electrons. EXAFS data concerning surface atoms can be derived from the spectrum observed by such a technique. This method is called surface EXAFS (or SEXAFS) and provides us with structural information that is complementary to that obtainable from low-energy electron diffraction (LEED).

In this paper, we describe first the present status of the experimental facilities regarding EXAFS and SEXAFS spectroscopy by use of synchrotron radiation, then present details of some of the important work which has been carried out using synchrotron radiation on the structures of catalysts and those of adsorbed layers on single-crystal surfaces, and finally we mention some of the work carried out by other techniques.

2. Experimental facilities for EXAFS and SEXAFS

Although EXAFS data could be obtained by use of a conventional in-laboratory X-ray source, the use of synchrotron radiation is of great importance for the purpose of applying EXAFS spectroscopy widely to the structural study of supported metal catalysts. In the case of a catalyst having a low content of supported metal, the EXAFS oscillation due to the supported metal used to appear with a low signal-to-background ratio, showing only a small edge jump even if the X-ray absorption edge of the metal were well separated from those of the elements contained in the support. In such a case, EXAFS data of sufficiently good quality is obtainable within a tolerable measuring time only by using synchrotron radiation. For SEXAFS experiments, the use of synchrotron radiation has a vital importance; first because there is no conventional soft X-ray source that can be used for the SEXAFS studies concerned with light elements; and second because the observation of X-ray polarization dependence is of great significance for the analysis of observed data.

In Japan, the use of synchrotron radiation for EXAFS spectroscopy started in 1982 when Photon Factory (PF-KEK) with a 2·5 GeV dedicated storage ring was established in the National Laboratory for High Energy Physics (KEK). The first beamline constructed for EXAFS spectroscopy was BL-10B, equipped with a double crystal monochromator using a channel-cut Si(311) crystal, the available photon energy being 6–25 keV with a resolution of $\Delta E/E = 10^{-4}$ (Oyanagi *et al.* 1984). A facility for X-ray absorption experiments by the transmission method is permanently installed at this beamline. A large number of EXAFS experiments on the structures of heterogeneous catalysts have been carried out by a variety of research groups at this beamline. The EXAFS studies of supported metal catalysts which are described in this paper were mostly carried out at this beamline. Another EXAFS facility was constructed later at BL-7C. This station is equipped with a double crystal Si(111) sagittal-focusing monochromator with fixed beam position, and covers the photon energy range of 4–20 keV. EXAFS experiments at the energy region higher than those covered by the above two beamlines have been carried out at BL-14A having a superconducting vertical wiggler (Satow *et al.* 1987). This beamline has a double crystal Si(553) monochromator and covers the energy region 22–82 keV.

An experimental facility for SEXAFS in the soft X-ray region was constructed at BL-11B (Ohta *et al.* 1986c). This is a windowless ultra-high vacuum (UHV) beamline

having a focusing mirror and UHV-compatible double-crystal monochromator, where InSb(111) and three other kinds of monochromating crystal can be interchanged without breaking the vacuum. The energy region covered by this monochromator is 1·7–3·8 keV, the resolution $\Delta E/E$ being about 2×10^{-4}. SEXAFS studies on S and Cl layers formed on metal crystal surfaces were carried out at this beamline by installing a compact UHV chamber having CMA, LEED, Auger electron spectroscopy (AES) and other facilities for surface characterization together with the inlet system for the reaction gas. Initially, the SEXAFS experiments were done by means of the Auger-electron detection mode. Later a compact UHV-compatible proportional counter was developed and installed into the above-mentioned UHV chamber to carry out SEXAFS experiments in the fluorescent X-ray detection mode (Funabashi *et al.* 1989 a). The signal-to-noise ratio was found to be markedly improved by employing the fluorescent X-ray detection mode, since the background due to the substrate could be effectively removed by using the energy resolution of the proportional counter. In fact, it was shown that EXAFS data good enough to be used for structural analysis could be obtained even at a very low coverage; down to 1/60 monolayer in the case of the S/Fe system. The use of a proportional counter has great merit also for the soft X-ray standing-wave experiment, which will be described later.

For the solid surface studies by use of synchrotron radiations in lower energy regions, two beamlines were later constructed in the Photon Factory by Kuroda and his collaborators at facilities belonging to the Research Center for Spectro-Chemistry (RCS) of the University of Tokyo (Namba and Kuroda 1986, Namba *et al.* 1989). These are BL-7A and BL-7B, which have a normal-incidence grating monochromator covering the energy range 10–50 eV and a grazing-incidence grating monochromator covering 10–1000 eV.

3. Structural studies on solid catalysts

3.1. *Attached metal catalysts*

The chemical surface design for solid catalysts is one of the most challenging subjects in catalytic chemistry. It is a promising way to create active surfaces with excellent catalytic properties as well as to elucidate reaction mechanisms, including details concerning the dynamic behaviour of active sites. The studies on the catalysts having chemically and structurally controllable surface systems are expected to offer novel information on the origins of catalysis when combined with structural information.

One of the ways to prepare such a catalyst is to use the chemical reaction of an organometal complex with the functional groups on the surface of the support. Catalysts having chemically attached Mo dimers were synthesized by Iwasawa *et al.* (1983) by using the reaction between Mo_2 $(\eta^3\text{-}C_3H_5)_4$ and the surface OH groups of silica, followed by chemical treatments with H_2 or O_2. Extensive structural investigations were performed on this catalyst by use of EXAFS spectroscopy, first by using an in-laboratory EXAFS spectrometer (Sato *et al.* 1982, Iwasawa *et al.* 1983a) and later by use of synchrotron radiation (Iwasawa *et al.* 1985a, b, 1986). The structural change in the process of catalysis was also investigated by means of *in situ* EXAFS experiments employing a specially devised flow-type reaction chamber.

From the analysis of the Mo K edge EXAFS data, the Mo–Mo separation in the Mo(II) dimer catalyst, in figure 1, was determined to be 2·80 Å, which was considerably larger as compared with the Mo–Mo separation of 2·183 Å in the original complex A.

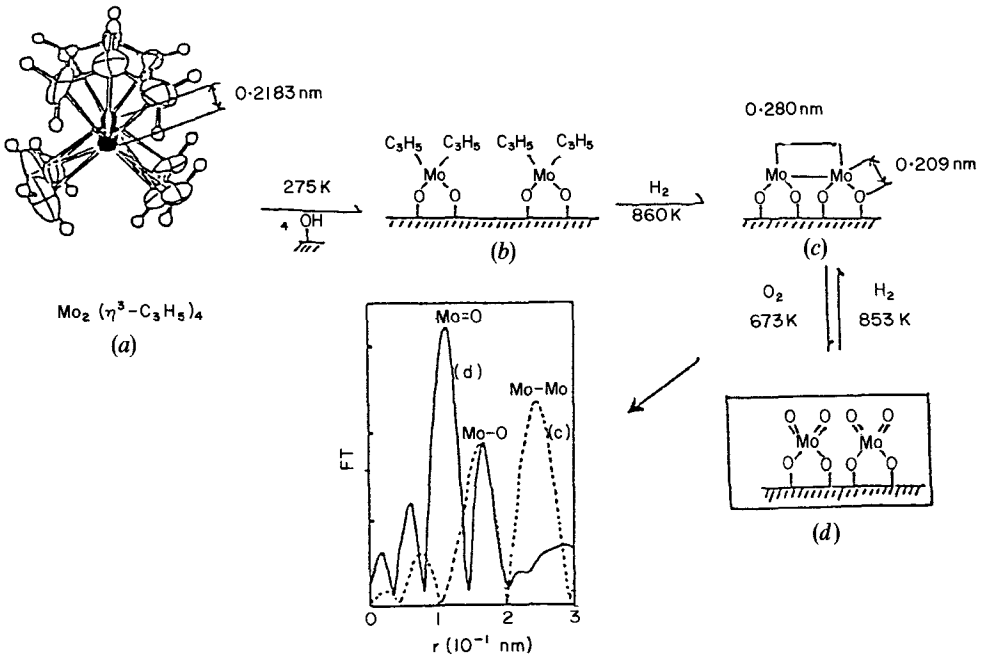

Figure 1. Structure of the attached Mo dimer catalyst prepared by the reaction of $Mo_2(\eta^3\text{-}C_3H_5)_4$ with surface OH groups of silica. The inset shows the Fourier transforms of the Mo K edge EXAFS.

The Mo–O (support) distance was found to be 2·09 Å. The values of the Mo–Mo and Mo–O (support) coordination numbers were determined to be about one and two respectively, in agreement with the expected structure shown in figure 1.

As shown in the inset of figure 1, the peak due to the Mo–Mo bond disappeared from the Fourier transform of the EXAFS oscillation when the catalyst was heated to 675 K in an oxygen atmosphere, and at the same time a new peak assignable to an Mo–O double bond appeared. The coordination number of Mo = O was determined to be about two, indicating the change to the structure (*d*). Conversely, when the Mo(VI) structure (*d*) was reduced with H_2 to the Mo(II) level at 853 K, the Mo = O peak disappeared from the Fourier transform with the concomitant appearance of the Mo–Mo peak. In these redox treatments the intensity of the Mo–O single-bond peak remained unchanged, as expected from the structures shown in figure 1.

The Mo dimer catalyst thus obtained was found to be more active for ethanol oxidation than a conventional Mo catalyst (Iwasawa and Tanaka 1984). The reaction kinetics and the stoichiometries of this ethanol oxidation reaction indicated that the catalytic reaction proceeds by the following two-stage redox mechanism:

$$Mo^{6+}\text{–}Mo^{6+} + C_2H_5OH \rightarrow Mo^{5+}\text{–}Mo^{5+} + CH_3CHO + H_2O, \quad (1)$$

(rate constant k_1)

$$Mo^{5+}\text{–}Mo^{5+} + \tfrac{1}{2}O_2 \rightarrow Mo^{6+}\text{–}Mo^{6+}. \quad (2)$$

(rate constant k_2)

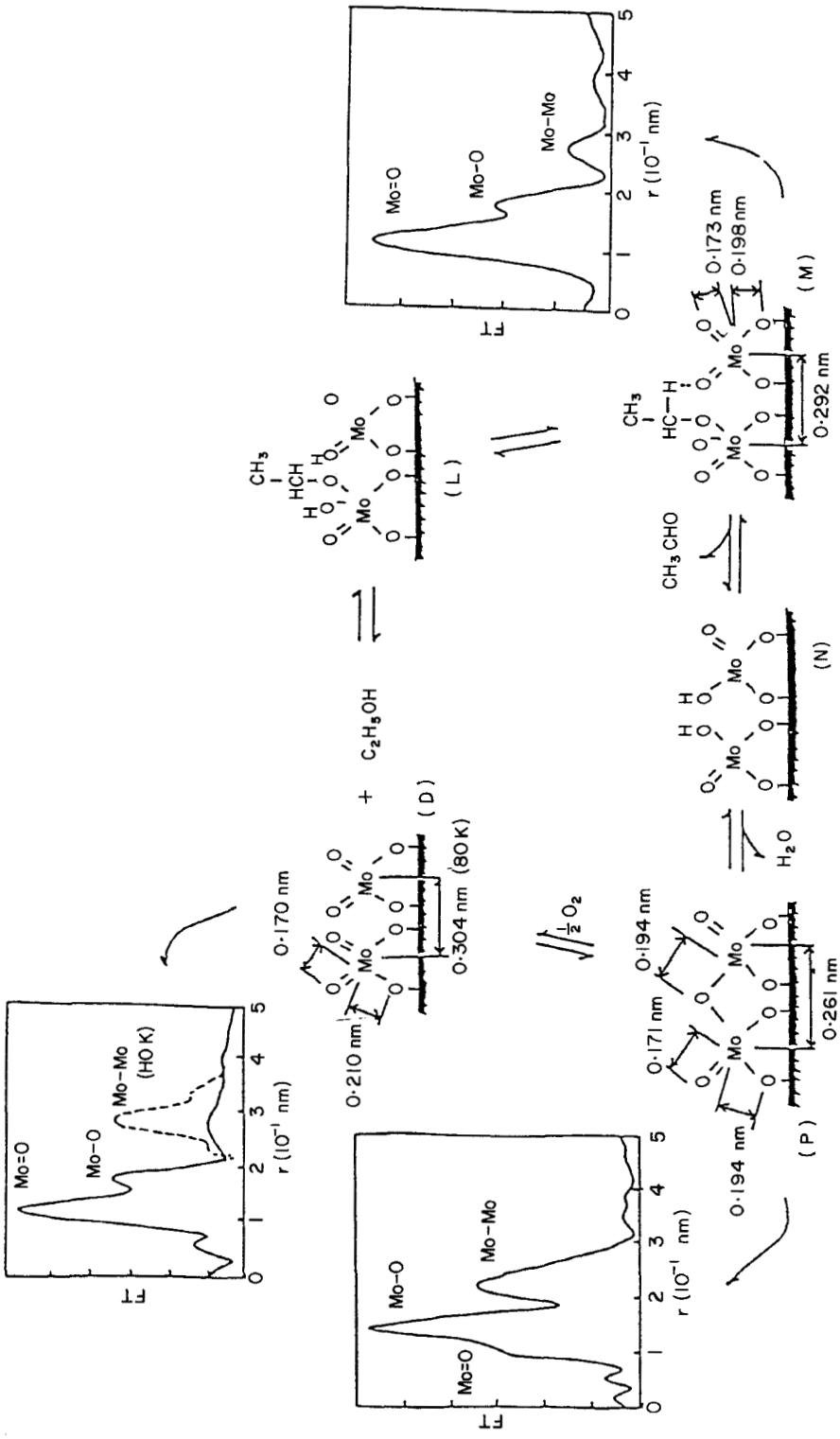

Figure 2. Structural charge of Mo dimers during ethanol oxidation. The insets show the Fourier transform of the Mo K edge EXAFS.

In a steady state the reaction rate r is expressed by equation (3):

$$P_E/r/(Mo_2)_0 = 1/k_1 + P_E/2k_2/P_{O_2} \quad (3)$$

$$k_1 = 3{\cdot}5 \times 10^{-21}\ \text{min}^{-1}\ \text{site}^{-1}$$

$$k_2 = 3{\cdot}7 \times 10^{-22}\ \text{cm}^{3/2}\ \text{step}^{1/2}\ \text{min}^{-1}\ \text{site}^{-1}$$

where $(Mo_2)_0$, P_E and P_{O_2} represent the amount of molybdenum dimers, the partial pressure of ethanol, and the partial pressure of oxygen respectively. The values of k_1 and k_2 as determined from the steady-state rate (equation (3)) agreed well with rate constants which were determined independently for step (1) and step (2). However, there remained a question as regards the reason why Mo dimers are so active. In order to understand the cooperative catalysis by the two adjacent Mo atoms, the structural changes undergone by the Mo dimers during the catalystic oxidation of ethanol were investigated by means of the *in situ* EXAFS technique (Iwasawa *et al.* 1986). The conclusion of this study is illustrated in figure 2 (Iwasawa *et al.* 1986, Iwasawa 1985, 1989). From the analysis of EXAFS data of the state D in figure 2, the Mo=O and Mo–O (support) distances were determined to be 1·70 and 2·10 Å respectively. Since there is no chemical bond between two Mo atoms at the adjacent sites, the Mo–Mo peak did not clearly appear in the Fourier transform of the room-temperature EXAFS data, but it did appear in the Fourier transform of the EXAFS data at 80 K, which gave an Mo–Mo distance of 3·04 Å. The species D reacted with ethanol to form an ethoxyl group in the state L, which must be hydrogen-abstracted by the molybdenum–oxygen double bond forming the intermediate state (the species M in figure 2). The Mo K edge EXAFS spectrum was observed for this state. The Fourier transform of the observed EXAFS data gave a peak due to the Mo–Mo bond with the distance of 2·92 Å, besides the peaks due to Mo=O and Mo–O (support) bonds. The appearance of an Mo–Mo peak in the room temperature data means that the Debye–Waller factor of the Mo–Mo in this state is relatively small, although there is no direct chemical bonding between the two Mo atoms. Seemingly this phenomenon is due to the formation of a bridge through the hydrogen bond between the methylene-hydrogen of the ethoxyl group and the double-bond oxygen of the adjacent Mo site, as illustrated by the structure M in figure 2. The above-mentioned Mo–Mo distance is shorter by 0·12 Å than that in the dioxomolybdenum dimer D. The analysis of the Mo K edge EXAFS data measured after the production of acetaldehyde and water gave the structure P in figure 2. The Fourier transform of the EXAFS data at this state showed a strong peak corresponding to an Mo–Mo bond. The Mo–Mo distance was found to be 2·61 Å, which is markedly shorter as compared with the intermediate species M. This fact indicated the formation of an Mo–O–Mo bridge between Mo atoms. It was confirmed from the EXAFS data that the above-mentioned Mo^{5+} dimers P were oxidized by oxygen to form the original dioxomolybdenum dimers D.

The mechanism including dynamic change of the structure of the active site was elucidated for the first time by this *in situ* EXAFS experiment (Iwasawa *et al.* 1985a, b).

SiO_2-supported Rh catalysts are known to be good catalysts for important reactions such as the synthesis of C_2-oxygenated compounds from syngas ($CO + H_2$) and alkene hydroformylation. The CO insertion reaction is an important key step in these catalytic reactions. Iwasawa and his collaborators synthesized a Rh dimer catalyst using the reaction of $[Rh(C_5Me_5)CH_3]_2(\mu\text{-}CH_2)$ with OH groups on a silica surface and studied the structural change of this catalyst by use of EXAFS and infrared spectroscopy (Kitamura-Bando *et al.* 1989, Asakura *et al.* 1989). From the

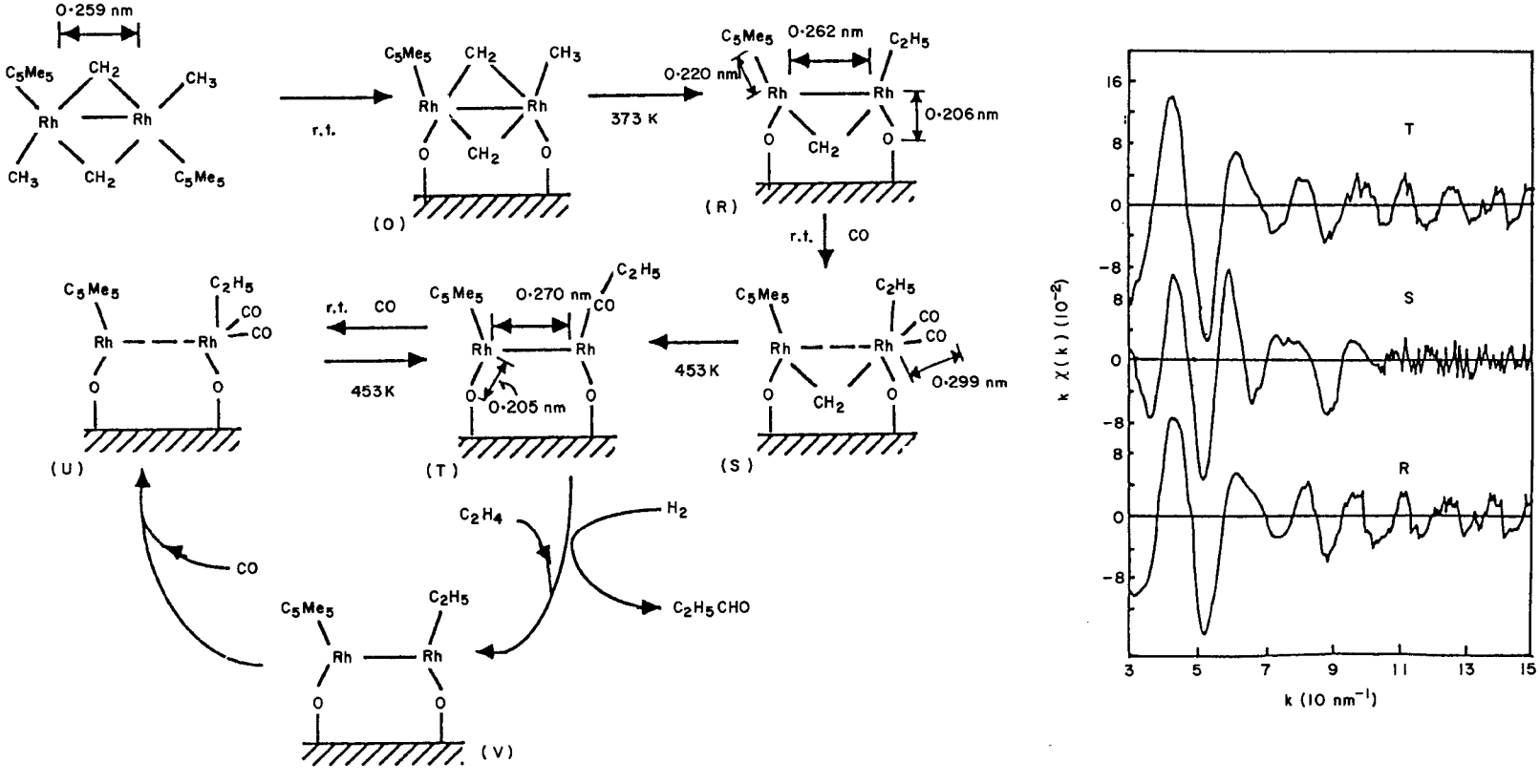

Figure 3. Structural charge of the SiO_2-attached Rh dimers related by *in situ* EXAFS study and catalytic cycle for ethene hydroformylation.

stoichiometry of the evolved gases and the change in infrared spectrum in the process of the synthesis of the catalyst, it was concluded that the precursor Rh dimer complex reacted with the surface OH groups, losing one CH_3 ligand and one C_5Me_5 ligand to give the structure O in figure 3. The infrared spectrum after the heat treatment to 373 K *in vacuo* showed that the remaining CH_3 ligand reacted with one of the μ-carbene groups to form a C_2H_5 ligand. By combining these items of information with the results of the analysis of Rh K edge EXAFS data, the structure was concluded to be the one shown as R in figure 3. The Rh–Rh, Rh–C and Rh–O (support) distances were determined to be 2·62, 2·20 and 2·06 Å respectively.

When the catalyst in the state R was exposed to CO, the CO adsorption took place in the stoichiometric ratio of two CO molecules per Rh dimer. The infrared spectrum of the catalysts in this state showed new bands at 2032 and 1969 cm^{-1}, which were assigned to the twin CO bands. On heating this catalyst to 423–473 K under vacuum, the infrared spectrum showed a new band at 1710 cm^{-1} with concomitant disappearance of the twin CO bands. The band due to carbene diminished greatly at this stage (T in figure 3). When the catalyst was again exposed to CO at room temperature, the twin CO bands were regenerated and at the same time the 1710 cm^{-1} band disappeared. This state was denoted as U in figure 3. The 1710 cm^{-1} band was assigned to the CO stretching vibration of the acyl (propanoyl) group attached to the Rh atom. The analysis of the Rh K edge EXAFS data of the state T gave the Rh–Rh distance of 2·70 Å, which is a little larger in comparison with the corresponding distances in the state R. The contribution of this Rh–Rh bond disappeared on changing to the state U by exposure to CO at room temperature, but appeared again on heating to 453 K *in vacuo*. On the basis of these observations by infrared and EXAFS spectroscopy, the states T and U were concluded to have the structures shown in figure 3. The change between these two states was confirmed to be completely reversible. Note that this change between T and U is just the reverse to that which is usually expected. Generally the CO insertion is known to proceed under the effect of a high pressure of CO. On the contrary, the change from the state U to the state T, which is a CO insertion reaction, takes place by heating under vacuum in the case of this Rh dimer catalyst. The formation and breaking of the Rh–Rh bond was considered to play an important role in this unique behaviour.

The Rh dimer catalyst mentioned above was shown to have a higher activity for ethene hydroformylation than that of conventional Rh catalysts. The selectivity toward propanol was about three times large than the latter. The catalytic cycle of this reaction is also shown in figure 3 (the cycle involving T, V and U). The metal-promoted CO insertion mechanism which was revealed by the above study seems to provide a new aspect of metal catalysis.

3.2. *Metal carbonyl cluster-derived catalysts*

The catalytic activity and selectivity of a supported metal catalyst are dependent on the dispersion state of the supported metal as well as on the metal–support interaction. Metal carbonyl clusters are often used as the precursor so as to enable the preparation of a catalyst having a highly and uniformly dispersed state of the supported metal. The use of a bimetallic carbonyl cluster as the precursor is a good way to control the dispersion of the two metals in a bimetallic catalyst. Ichikawa studied the catalytic properties of the catalysts derived from Rh carbonyl clusters and those derived from Rh–Co bimetallic carbonyl clusters (Ichikawa 1978, Ichikawa 1979). He showed that

the catalytic properties of the catalysts derived from Rh carbonyl clusters were strongly affected by the nature of the metal oxide support, such as La_2O_3, TiO_2, ZnO and MgO. He also showed that the activity and selectivity of a catalyst derived from an Rh–Co carbonyl cluster could be controlled by changing the Rh:Co ratio in the original carbonyl.

Structural studies by EXAFS spectroscopy were carried out on the catalysts derived from a variety of metal carbonyl clusters such as $Fe_3(CO)_{12}$ (Iwasawa *et al.* 1983b), $Co_2(CO)_8$ (Iwasawa *et al.* 1984), $Ru_3(CO)_{12}$ (Asakura *et al.* 1985, Asakura *et al.* 1986a), $Rh_6(CO)_{16}$ (Asakura *et al.* 1986b). $Rh_2Co_2(CO)_{12}$ (Yokoyama *et al.* 1984) and $RhCo_3(CO)_{12}$ (Yokoyama *et al.* 1984). In most cases, the catalysts were found to have very small metal clusters retaining more or less the structure similar to that of the metal cluster skeleton of the original carbonyl molecule, the formation of M (metal)–O (support) bonding being often observed. As an example of those studies, the structural changes in the process of carbonyl-impregnation, heat-treatment under vacuum and final reduction with hydrogen, are shown in figure 4 for the catalysts derived from $Ru_3(CO)_{12}$ (Asakura *et al.* 1986a). On V_2O_5, SiO_2 and TiO_2, metal carbonyl molecules are physically adsorbed without forming a chemical bond with the support, but $[HRu_3(CO)_{11}]^-$ is formed when the carbonyl is adsorbed on supports of high basicity, such as MgO and Al_2O_3 containing K. The bonding state of the Ru atom after H_2 reduction was found to be significantly different between the two cases; very small metallic Ru clusters are formed on V_2O_5, SiO_2 and TiO_2, while thin raft-like clusters with Ru–O (support) bonding are formed on Al_2O_3 and MgO.

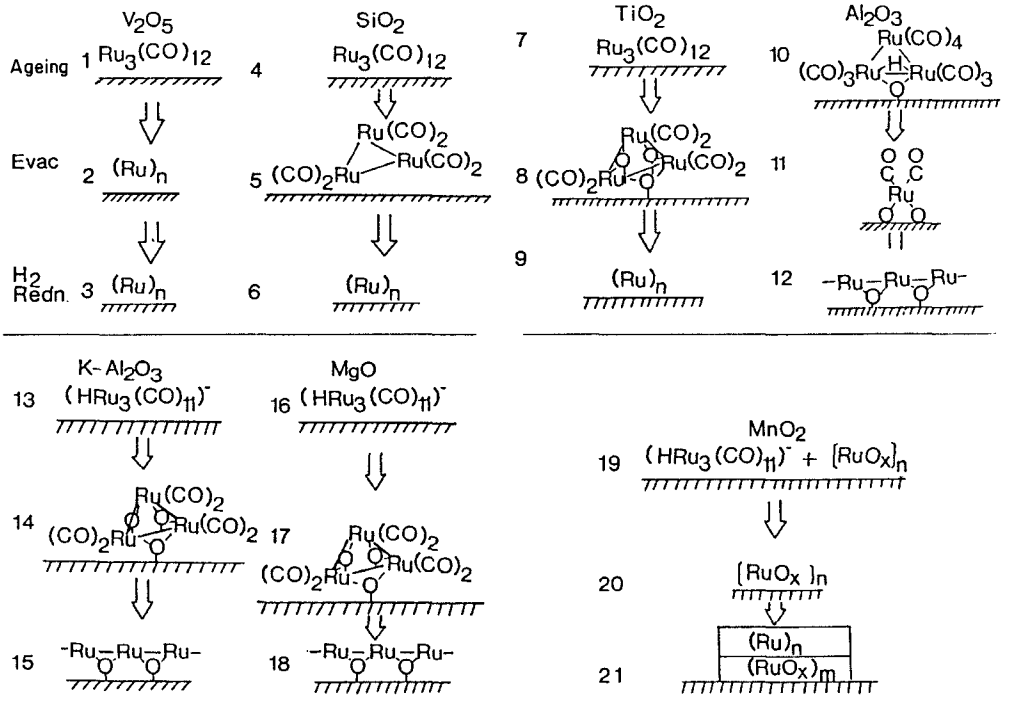

Figure 4. Structural difference of Ru catalysts derived from $Ru_3(CO)_{12}$ supported on metal oxides.

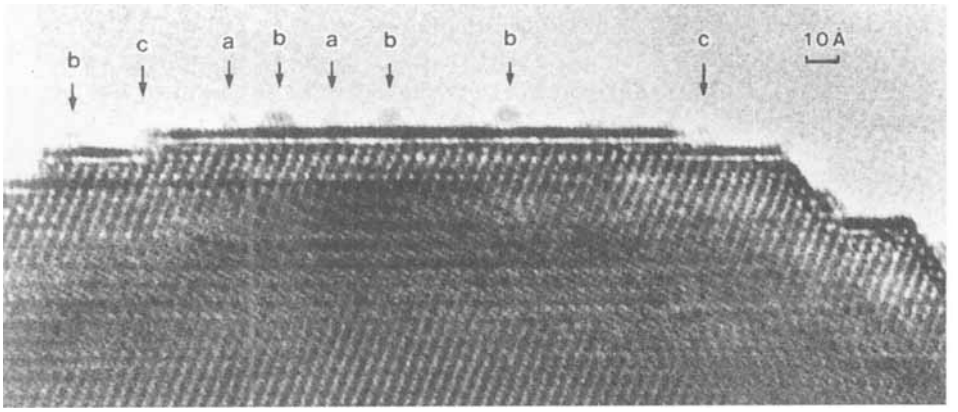

Figure 5. High-resolution electron micrograph of Rh clusters supported on an ultra-fine particle of an Al_2O_3 single crystal. The top flat surface is Al_2O_3(111). Two types of Rh cluster (a and b) can be seen at the positions indicated with arrow.

A direct electron microscope observation of the Rh clusters which were produced from $Rh_6(CO)_{16}$ on the surface of Al_2O_3 was performed by Iijima and Ichikawa (1985) by use of a high-resolution electron microscope. They put carbonyl molecules on the surfaces of ultra-fine spherical particles of single-crystal alumina (diameter 5–80 nm), and carried out observations using a high-resolution electron microscope having special devices for the observation of ultra-fine particles. One of the electron micrographs reported by them is reproduced in figure 5. The top flat surface of the particle in this photograph was assigned to the (111) face of Al_2O_3 from the observed lattice image. The hemispherical particles indicated with an arrow are Rh clusters supported on this surface. There are two types of cluster, which are labelled a and b, respectively. The diameter of the cluster a is about 6 Å and that of the cluster b is about 10 Å. The former is close to the diameter of Rh cluster skeleton in the original carbonyl molecule. The latter is likely to be the cluster containing more than six Rh atoms. Some of the clusters are located at the steps (labelled c), but there is no indication for the clusters being attached preferentially at the step.

3.3. *Supported metal catalysts*

Structural study by EXAFS spectroscopy has been performed on a variety of catalysts prepared by the conventional impregnation method. Since it is impossible to take up all of them we will describe here two topics among those investigations; the reversible phase change of Cu cluster on ZnO (Tohji *et al.* 1985) and the investigation of the strong metal–support interaction (SMSI) state by means of the analysis of the temperature dependence of the EXAFS spectrum (Yokoyama *et al.* 1989c).

The Cu/ZnO catalyst containing alumina or chromia is industrially important for methanol synthesis from H_2 and CO. On this catalyst, Tohji *et al.* studied the structural change of Cu clusters under conditions close to those pertaining in the reaction vessel under a H_2 stream at elevated temperature (Tohji *et al.* 1985). This *in situ* EXAFS experiment was carried out by use of an in-laboratory EXAFS apparatus (Tohji and Udagawa 1984). The Cu/ZnO catalyst was prepared by a co-precipitation method; the

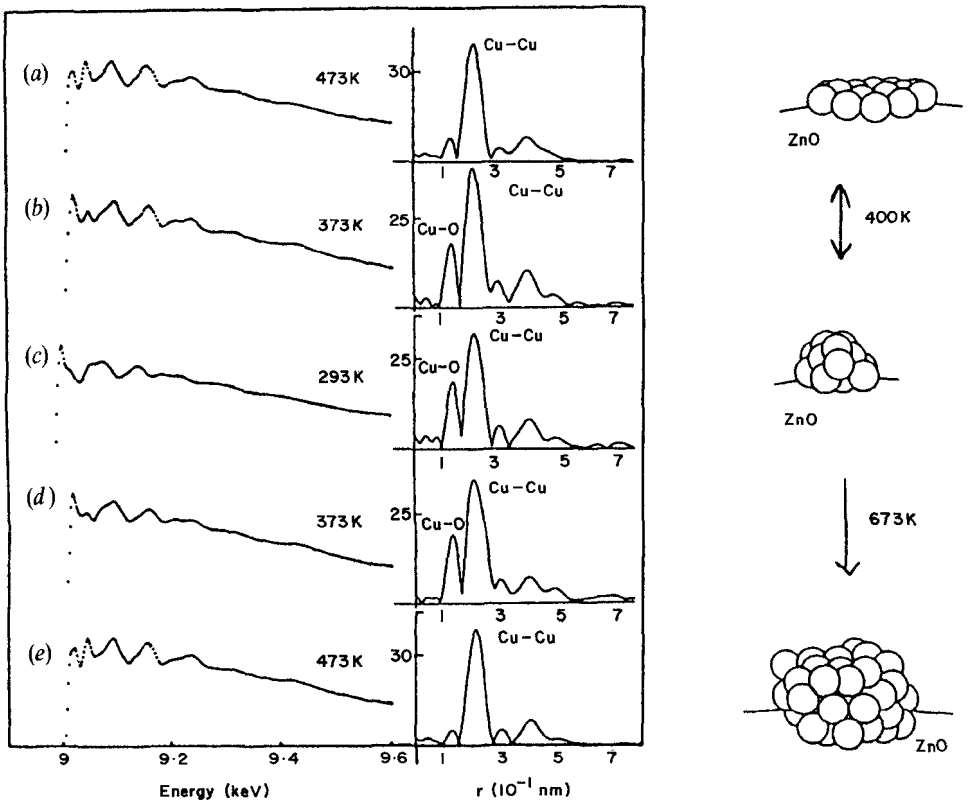

Figure 6. Cu K edge EXAFS spectra and their Fourier transforms of a Cu/ZnO catalyst reduced at 473 K. The EXAFS spectra were observed by changing the temperature in the order 473 K→373 K→293 K→373 K→473 K under a constant H_2 flow. The drawing on the right-hand side of this figure illustrates the observed structural change.

precipitate (Cu:Zn = 3:7) was dried overnight at 383 K, followed by calcination at 623 K for 3 h, and then reduced at given temperatures under a H_2 stream. The Cu K edge EXAFS spectra of the reduced catalyst subsequently observed at 473, 373, 293, 373 and 473 K under a constant H_2 flow are shown in figure 6 together with their Fourier transforms. Note that the Fourier transform showed only one prominent peak at 474 K while it showed two prominent peaks at both 293 and 373 K. This change was found to be completely reversible on repeating heating/cooling cycles.

A detailed analysis of the EXAFS data showed that, among the two peaks in the Fourier transform of the EXAFS data measured at 293 or 373 K, the one corresponding to the shorter distance could confidently be ascribed to Cu–O and the other at a larger distance was due to Cu–Cu, the coordination number being determined to be about one for Cu–O and six for Cu–Cu. The prominent peak in the Fourier transform of the EXAFS data at 473 K is due to Cu–Cu, the coordination number being determined to be about ten. Once the catalyst was heated to above 600 K in H_2, an irreversible change took place. The EXAFS data for this state was found to be very much the same as that of the bulk Cu metal, giving a Cu–Cu coordination number of about twelve. Tohji *et al* (1985) proposed the structure model shown in figure 6. Namely, at lower temperature, Cu atoms form a quasi-two-dimensional layer over the ZnO surface, involving Cu–O bondings, but this Cu layer changes to a small metal

particle when the temperature is elevated to above 400 K. The phase change between these two states was reversible as already mentioned. At a temperature above 600 K, the Cu clusters coalesced to form larger particles having a diameter of about 20–30 Å. They considered that the reversible transformation between the two-dimensional and three-dimensional forms became impossible once the particle size exceeds some threshold. The phenomenon mentioned above might well be an explanation for the known loss of catalytic activity through overheating.

It is well known that the H_2 and CO absorption capacities of noble metal catalysts supported on a reducible transition metal oxide, such as TiO_2, dramatically decrease when the catalysts are reduced by heating to high temperature in H_2. Since this phenomenon was ascribed to the strong interaction between the supported metal and support, it was called 'strong metal–support interaction' (SMSI). Yokoyama *et al.* (1989c) derived structural information on the SMSI state from the study of the temperature dependence of the EXAFS data. On the Rh(2·0 wt%)/SiO_2 and Pd(2·0 wt%)/SiO_2 catalysts having an average metal particle size of about 30 Å, they observed the Rh K edge (or Pd K edge) EXAFS at various temperatures over the range of 25–355 K for the normal and SMSI states. The EXAFS oscillation due to Rh–Rh (or Pd–Pd) was analysed by means of the cumulant expansion technique to derive the mean-square relative displacement (MSRD) of the metal–metal bond.

The values of the MSRD thus obtained on the Rh/SiO_2 catalyst are shown in figure 7 together with the corresponding data for the bulk Rh metal. The temperature dependence of the thus determined MSRD was analysed to give an estimate of the

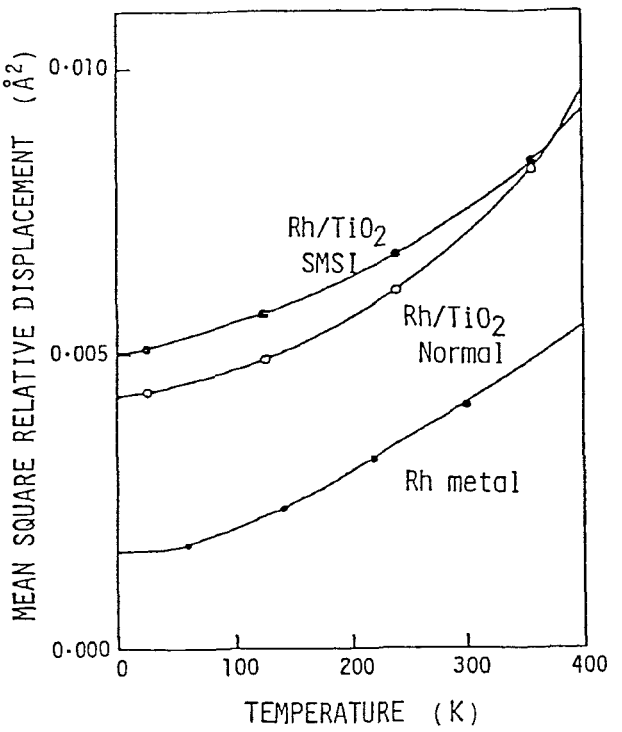

Figure 7. Mean-square relative displacement (MSRD) of the Rh–Rh bond derived from the temperature dependence of the Rh K edge EXAFS of the Rh/SiO_2 catalyst.

Table 1. Debye temperature of supported Rh and Pd metal particles and bulk metals determined by EXAFS.

State		Rhodium	Palladium
Average	'SMSI'	354 K	273 K
	'Normal'	316 K	248 K
Surface	'SMSI'	341 K	241 K
	'Normal'	241 K	127 K
Bulk metal		362 K	282 K
Single-crystal surface determined by LEED		260 K	142 K

Debye temperature of the supported metal. The results of this analysis are given in table 1. Note that the average Debye temperature is considerably higher in the SMSI state than in the normal state. The Debye temperature of the atoms on the surfaces of supported metal particles was estimated from the average Debye temperature by assuming that the Debye temperature of the atoms inside the metal particle is the same as that of the bulk metal. These results are also shown in table 1. Both in Rh/SiO_2 and in Pd/SiO_2, the surface Debye temperature thus estimated for the normal state agreed well with the corresponding values reported for the atoms of the single-crystal surface of the metals, but was markedly higher in the SMSI state, indicating that the surface of the metal particles was strongly covered by some chemical species. This result provides evidence supporting the decoration model of the SMSI state. The use of the temperature dependence of the EXAFS in the structural study of catalysts has been further explored by Yokoyama *et al.* (1986, 1989a, b).

4. Structural studies on single-crystal surfaces

4.1. *The soft X-ray standing wave method*

According to the dynamical theory of X-ray diffraction, an X-ray standing wave field is generated in a highly perfect crystal under the diffraction condition by the interference of the incident and diffracted X-rays. The location of the node of this standing wave field moves as the orientation of the sample crystal is slightly varied within the angle range satisfying the diffraction condition. Since the probability of X-ray absorption will be minimum when an atom is at the node of the standing wave and maximum when it is at the loop, the intensity of the X-ray fluorescence (or that of the electron emission) varies accompanying the movement of the node of the standing wave field, which results in a modulation of the intensity of X-ray fluorescence (or electron emission) when the intensity is recorded as a function of the orientation of the sample crystal. This is called the standing wave (SW) profile. In the case of a crystal containing foreign atoms implanted into the lattice, the SW profile of the X-ray fluorescence emitted from the implanted atoms will differ more or less from that of the X-rays emitted from the atoms of the host crystal lattice, depending on the location of the implanted foreign atoms relative to the host crystal lattice. Thus the location of a foreign atom can be determined from the analysis of the observed SW profiles.

The use of this technique was first demonstrated by Golvochenko *et al.* (1974) in the cases of As atoms implanted into a Si single crystal. It was also applied for determining the location of ad-layers such as Br/Si(111) (Golvochenko *et al.* 1982, Materlik and Zegenhagen 1984, Materlik *et al.* 1984) and Br/Ge(111) (Bedzyk and Materlik 1985). All

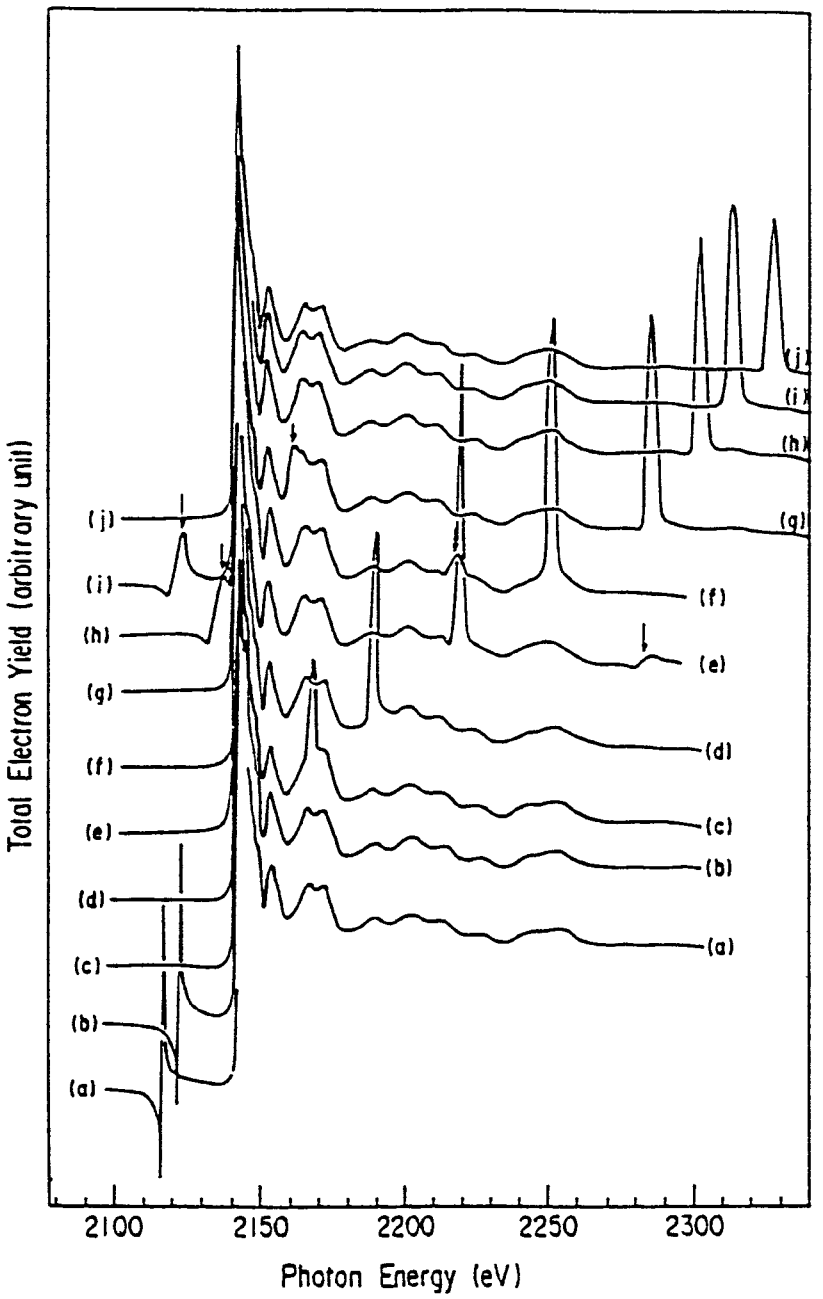

Figure 8. Total electron yield spectra of InP, observed for different X-ray incident angles: the Bragg angle is (*a*) 90°, (*b*) 85·5°, (*c*) 77·5°, (*d*) 75·0°, (*e*) 72·5°, (*f*) 70·0°, (*g*) 67·5°, (*h*) 67·0°, (*i*) 66·0° and (*j*) 65·0°. The sharp structure whose position varies with the incident angle is the signal due to standing wave.

of these SW experiments were done by use of hard X-rays. In the case of the SW experiment with hard X-rays, the sample needs to be a very perfect single crystal with an extremely flat surface. It is also necessary to use a very precise goniometer and a well collimated monochromatic X-ray beam, since the change of the sample orientation required for the observation of the SW profile is extremely small. These experimental requirements in the SW experiment with hard X-rays put some limit on its application.

Ohta *et al.* (1985) found that the structures due to standing wave appeared in the total-electron yield spectrum of InP shown in figure 8, where the SW structures are seen as sharp peaks. The shapes of the observed structures were found to be in good agreement with those calculated by the dynamical theory. The above finding indicated that the SW profile can be obtained in a very simple way by measuring the intensity of emitted electrons (or fluorescent X-rays) as a function of photon energy instead of rotating the sample crystal. Furthermore, it was found that the constraints required on the perfectness of crystal and the flatness of crystal surface are significantly less severe in the case of soft X-rays in comparison with the SW experiments with hard X-rays, since the X-ray incident direction can be made nearly normal to the reflecting plane. Accordingly, the SW profile can be measured even on a mosaic crystal whose SW profiles are difficult to obtain by use of hard X-rays. On the basis of these findings, Ohta *et al.* (1986b) proposed for the first time the possibility of a wide use of the soft X-ray standing-wave (SX-SW) method for the structure analysis of solid surfaces. It is the great advantage of this method that the observation of the SW profile can be carried out by use of the same apparatus as that for the SEXAFS experiment, hence SEXAFS and standing wave data can be measured on the same sample under the same conditions. This makes it possible to combine the structural information obtainable by the two techniques to elucidate surface structure.

In the SW experiment, it is of great significance to separate the SW profile characteristic of adsorbed atoms from those due to the substrate. This can be achieved by employing the method to detect the fluorescent X-rays characteristic of each element. A series of experiments done by Ohta and his collaborators have proved the usefulness of combining SEXAFS and standing wave methods to elucidate the structures of solid surfaces with a chemisorbed layer.

To illustrate the use of the above technique, we will show here the results obtained on c(2 × 2)Cl/Ni(100) (Yokoyama *et al.* 1989d). The Cl K edge EXAFS data were measured for three different X-ray incident angles (90°, 45° and 15°) and the SW profile associated with the Ni(200) reflection was measured for Cl Kα. From the analysis of Cl K edge EXAFS data, the adsorbed Cl atom was concluded to be at the fourfold hollow site on the Ni(100) surface and the Cl–Ni distance was determined to be 2·43 Å. From these data, the separation between the Cl atoms and the plane of the top Ni atoms was calculated to be 1·67 Å. On the other hand, the analysis of the Cl Kα SW profile shown in figure 9 showed that the Cl atoms were located at $1{\cdot}90 \pm 0{\cdot}04$ Å above the Ni(100) plane. The latter is larger by 0·13 Å than the separation of the Cl atoms from the plane of the top Ni atoms determined from EXAFS. It should be noted that the value from SW profiles is the one with respect to the Ni(100) plane in the bulk Ni lattice, which is responsible for the SW field, while the EXAFS result is to be regarded as the actual separation measured from the top Ni atom layer. Thus the difference gives the expansion of the spacing between the top and second Ni atom layers. In this way, the spacing between the top and second Ni atom layer was estimated to be 1·89 Å, which corresponds to an expansion by 7% from the bulk spacing. The structure thus concluded is shown in figure 10.

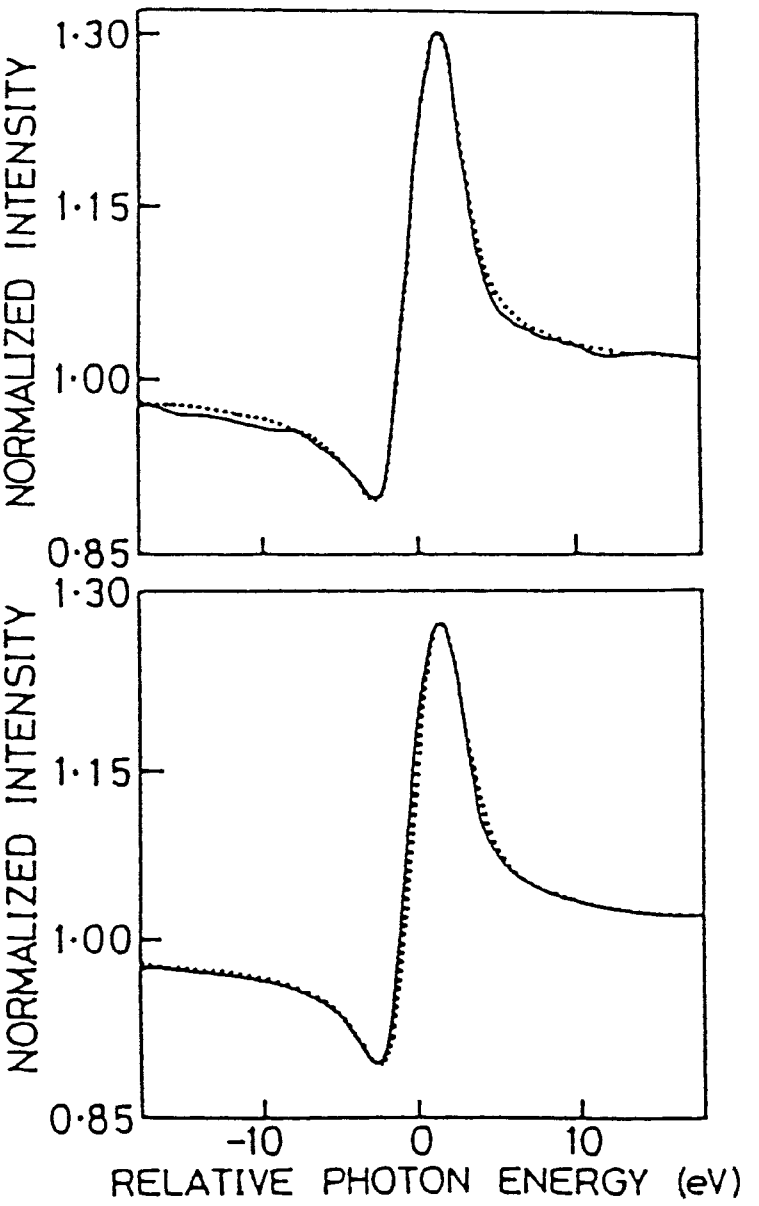

Figure 9. SW profiles observed on c(2 × 2)Cl/Ni(100): (*a*) Cl K_2 fluorescent X-ray yield; and (*b*) total electron yield, corresponding to SW profile for Ni lattice. (——) observed and (– – –) calculated profiles.

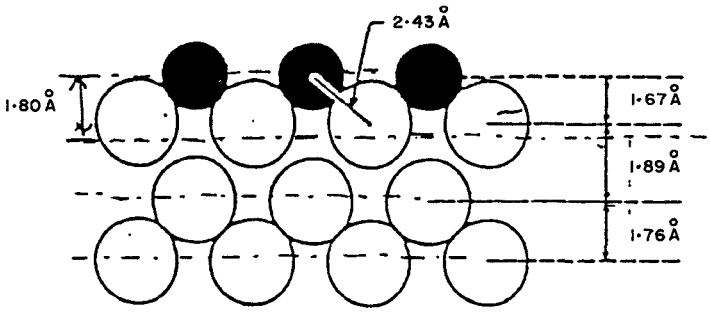

Figure 10. Structure of c(2 × 2)Cl/Ni(100), concluded from SEXAFS and SW studies.

4.2. *Structures of S/Ni (crystal) systems*

The chemisorption of sulphur on the surface of a transition metal is of great interest in connection with the poisoning effect of sulphur chemisorption on the catalytic activities of supported metal catalysts involving transition metals. Extensive studies by LEED and other techniques have been carried out with the S overlayers formed on the surfaces of metal single crystals, but many aspects remain to be elucidated. In the case of the S/Ni system, the sulphur adsorption behaviour is known to be different on different crystal faces of Ni, and also it is known that several different phases can be formed on the same crystal face depending on the dose of S and temperature. To elucidate the bonding between an adsorbed S atom and Ni atoms and the nature of the reorganization accompanying S chemisorption, Ohta, Kuroda and their collaborators have carried out structural studies employing SEXAFS and SW methods on the systems c(2 × 2)S/Ni(100), c(2 × 2)S/Ni(110), p(2 × 2)S/Ni(111) and also on ($5\sqrt{3}$ × 2)S/Ni(111) as well as on an S/Ni(7 9 11) stepped surface. All the experiments were done at BL-11B of PF-KEK. Here we will take up the two cases c(2 × 2)S/Ni(110) and ($5\sqrt{3}$ × 2)S/Ni(111) to illustrate the procedures involved in determining the surface structure (Ohta *et al.* 1986c, Kitajima *et al.* 1986, 1989, Yokoyama *et al.* 1989e, Funabashi *et al.* 1989b, Takata *et al.* 1989).

The S K edge spectra were measured on c(2 × 2)S/Ni(110) by use of the method detecting S KLL Auger electrons, the measurements being done for three different X-ray incident angles (measured from the crystal face), of $\theta = 90°$, 45° and 10° for two different directions of X-ray polarization $\phi = 0°$ and 90°, ϕ being the angle between the $\langle 1\bar{1}0 \rangle$ axis of Ni and the polarization plane of the X-rays (Ohta *et al.* 1986c). The observed spectra are shown in figure 11. It should be noted that the observed spectrum considerably differs depending on the incident angle and polarization of X-rays, in particular in X-ray absorption near-edge structure (XANES) region. The analysis of the EXAFS oscillation responsible for the main peak in the Fourier transform was first done with the one-shell model, which gave the results shown in table 2. Note that the S–Ni distance obtained significantly varied depending on the X-ray incident angle θ. This was concluded to be due to the situation that the EXAFS oscillation was in reality composed of the contribution of the four top-layer Ni atoms (denoted as Ni(T) in figure 12) and a second-layer Ni atom (Ni(B) in figure 12) which is located just below the S atom. The observed dependence of the effective coordination number on the incident angle and polarization direction were all successfully understood by the above model. Since the contribution of S–Ni(B) to the EXAFS must disappear in the case of normal

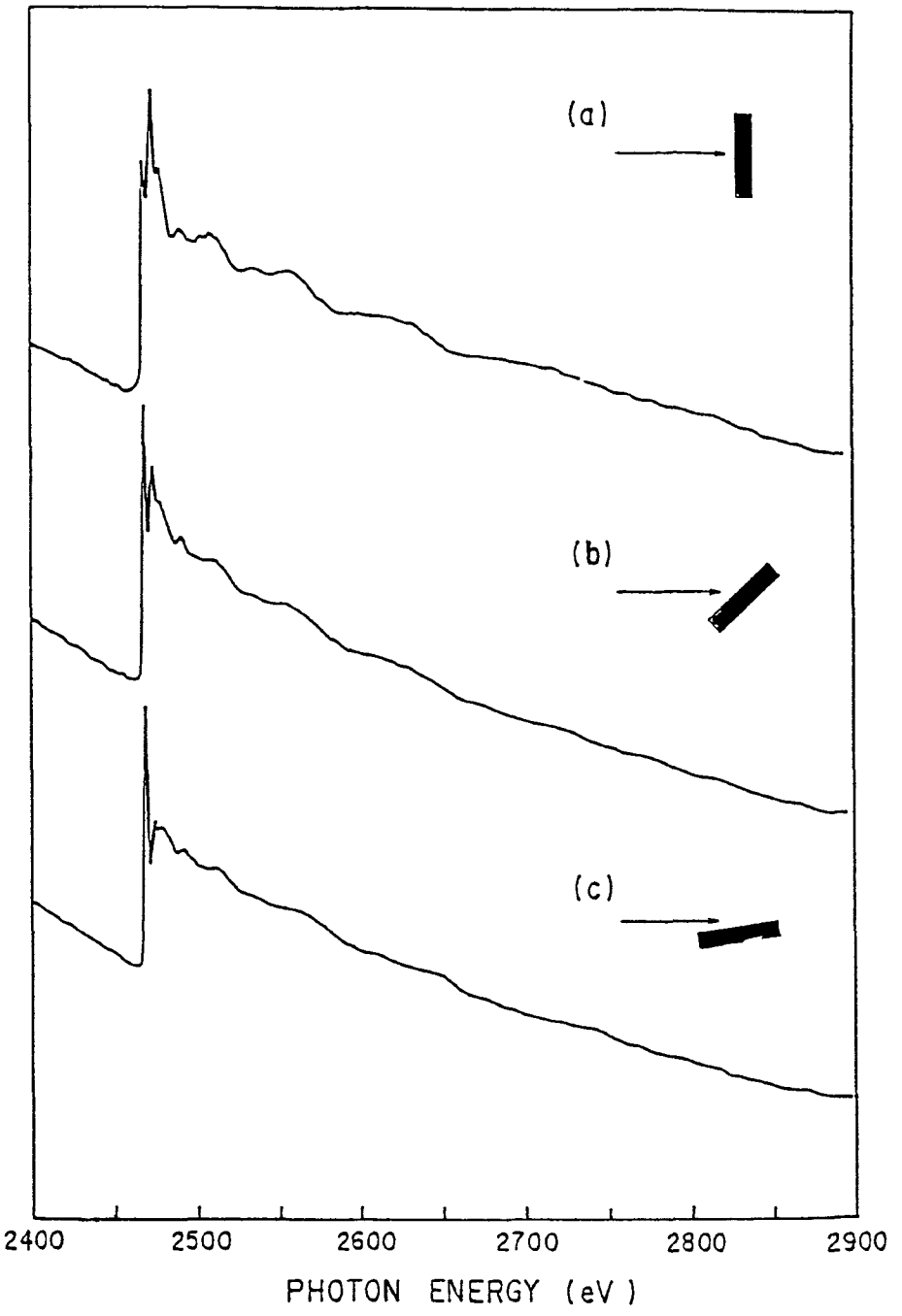

Figure 11. S K edge SEXAFS spectra of c(2 × 2)S/Ni(110) observed for different X-ray incident angles: (*a*) 90°, (*b*) 45° and (*c*) 15°.

Table 2. Results of the curve-fitting analysis of EXAFS data of c(2 × 2)S/Ni(110).

Polarization direction	Incident angle θ (degrees)	S–Ni distance (Å)	Effective coordination number N^*
⟨100⟩	90	2·31	5·83
	45	2·28	4·58
	10	2·22	3·69
⟨110⟩	90	2·31	2·74
	45	2·26	2·55
	10	2·24	3·45

incidence, the S–Ni distance obtained from the normal-incidence EXAFS data gives the S–Ni(T) distance. The EXAFS data obtained for grazing incidence were analysed with the two-shell model, one shell for four Ni(T) atoms and the other shell for one Ni(B) atom. Those analyses gave the S–Ni(B) distance to be 2·19 Å. In this way, the S–Ni distance was concluded to be 2·31 and 2·19 Å for Ni(T) and Ni(B) respectively. From these S–Ni distances, it was concluded that the S atom was located at 0·82 Å above the plane of Ni(T) atoms, and the spacing between the plane of Ni(T) and that of Ni(B) was 1·37 Å while the corresponding spacing in the bulk Ni crystal is 1·246 Å. This means that the spacing expands by 10% accompanying the S chemisorption. The structures of the S/Ni systems determined by SEXAFS are summarized in figure 13.

The behaviour of Ni(111), which is the most closely-packed atomic plane of the Ni crystal, is quite different from that of other faces of the Ni crystal. S absorption on Ni(111) gives various different phases other than p(2 × 2)S/Ni(111), namely the phases which give low-energy electron diffraction (LEED) patterns such as $(\sqrt{3} \times \sqrt{3})$R30, $(5\sqrt{3} \times 2)$ and $(8\sqrt{3} \times 2)$. Since LEED patterns such as $(5\sqrt{3} \times 2)$ and $(8\sqrt{3} \times 2)$ are complicated, it is difficult to determine S adsorption sites from analyses of the LEED

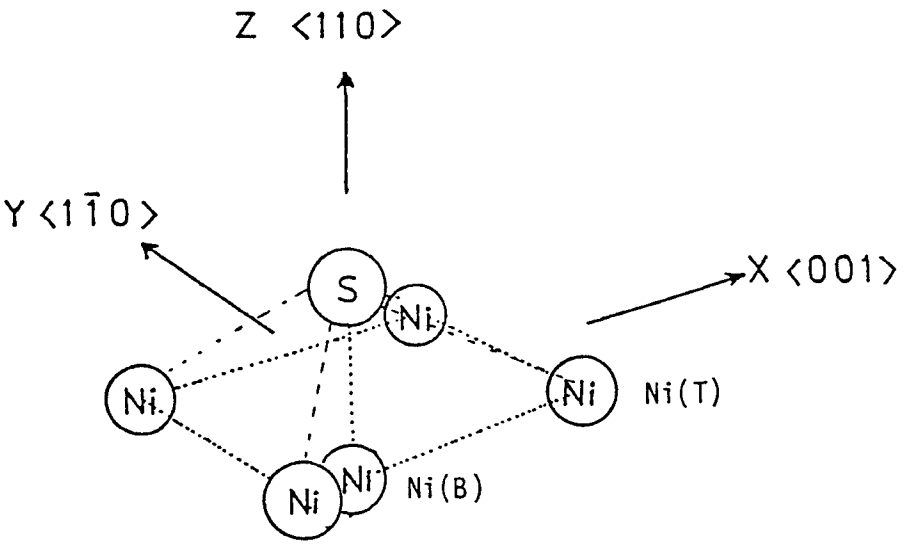

Figure 12. Model for the S absorption site c(2 × 2)S/Ni(100).

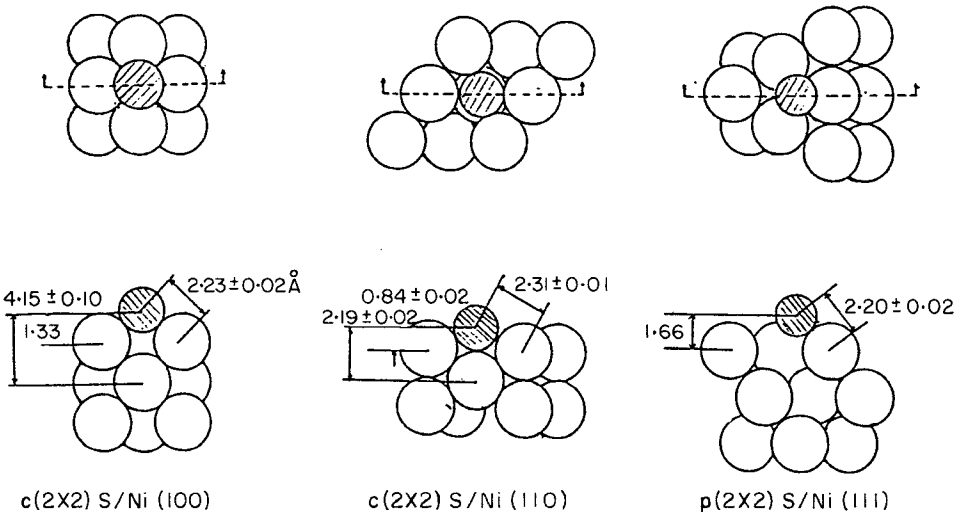

Figure 13. Local structures surrounding the S atom, concluded from the analysis of S K edge SEXAFS data. The values indicated in the figure are the atomic distances in Ångström units.

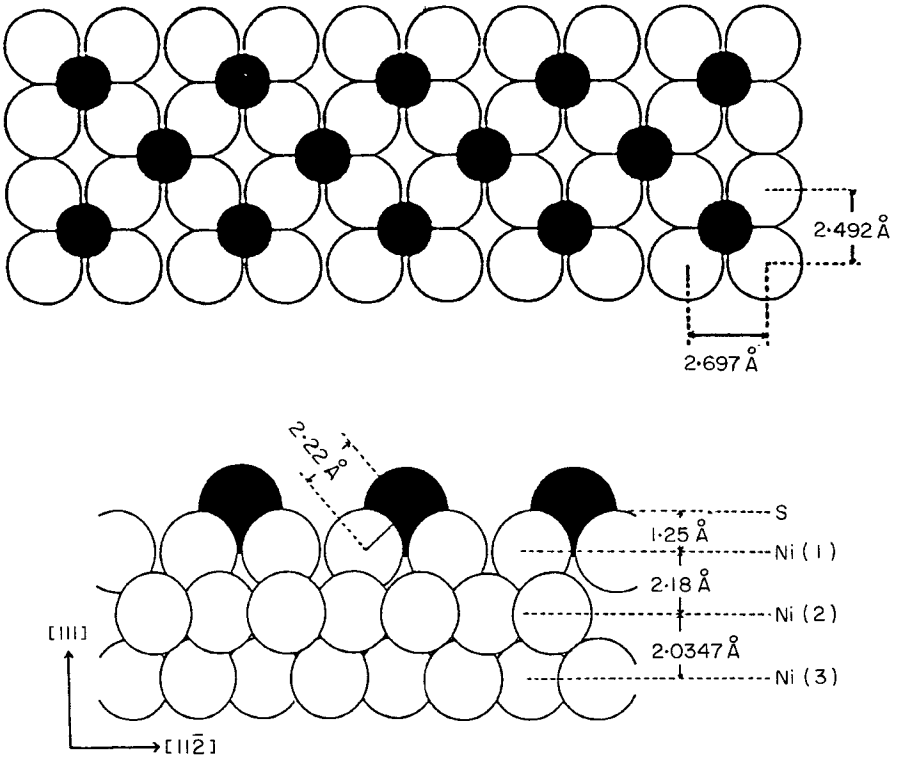

Figure 14. The structure of $(5\sqrt{3} \times 2)$S/Ni(111) derived from SEXAFS and SW experiments.

Table 3. Effective coordination number N^* (θ), their ratio $c(\theta)=N^*(\theta)/N^*(90°)$ and the direction of the S–Ni bond, determined for $(5\sqrt{3}\times 2)$S/Ni(111).

		Calculated			
	Observed	Proposed	Threefold	Bridge	On-top
$N^*(90)$	5·11	4·106	1·890	0·943	0·000
$N^*(45)$	4·62	3·947	3·555	2·529	1·500
$N^*(15)$	4·48	3·810	4·996	3·902	2·799
$c(45)$	0·904	0·961	1·811	2·682	∞
$c(15)$	0·877	0·928	2·643	4·139	∞
$\omega(45)$	32·4°	34·2°	49·6°	55·9°	90·0°
$\omega(15)$	33·4°	34·2°	49·6°	55·9°	90·0°

pattern only. Edmonds *et al.* (1971) suggested the reconstruction of the top Ni layer into a pseudo-Ni(100) surface in order to account for the observed $(5\sqrt{3}\times 2)$ and $(8\sqrt{3}\times 2)$ LEED patterns, but without evidence for it. SEXAFS study on this phase was carried out by Kitajima *et al.* (1989). The analysis of the EXAFS data of the $(5\sqrt{3}\times 2)$S/Ni(111) system gave a nearest S–Ni distance of $2{\cdot}22\pm 0{\cdot}03$ Å. The effective coordination numbers $N^*(\theta)$ obtained from the EXAFS data measured at the X-ray incident angle θ, their ratios $c(\theta)=N(\theta)/N(90°)$, and the angle of the S–Ni bond with respect to the surface $\omega(\theta)$ estimated from $c(\theta)$, are listed in table 3 together with the values calculated for various possible models. The observed EXAFS data were concluded to give the model where S atoms are on the fourfold sites of a reorganized pseudo-c(2 × 2) Ni layer as shown in figure 14. The SW experiment was also carried out on this system (Takata *et al.* 1989). The result of the analysis of the observed SW profile indicated that the adsorbed S atom was located at 1·40 Å above the Ni(111) plane, whereas it should be 2·20 Å for on-top, 1·84 Å for bridge and 1·69 Å for threefold hollow site. Thus the value observed from SW experiment cannot be understood without considering a marked reorganization in the top Ni atom layer. The location of the S atom was calculated to be 1·25 Å above the top Ni atom layer according to the proposed reconstructed model shown in figure 14. By combining this with the result of the SW experiment, the spacing between the top and second Ni layer was concluded to be 2·18 Å, which corresponds to a slight expansion from the corresponding spacing in the bulk Ni lattice (Takata *et al.* 1989).

4.3. *Structural studies by LEED, EELS and other techniques*

4.3.1. *NH_3–CO mixed overlayers on Ru(001)*

To reveal the mechanism of chemical reactions on solid surfaces, the nature of intermolecular interactions of neighbouring adspecies and their roles or effects on surface chemical processes should be clarified, since many catalytic reactions at steady state proceed on surfaces which are crowded with different kinds of adspecies. Interesting results were recently obtained by Sasaki *et al.* (1989) on the system where NH_3 and CO were co-adsorbed on Ru(001), from the use of LEED, high-resolution electron energy-loss spectroscopy (HREELS) and other techniques.

The CO adsorption on Ru(001) is known to give a series of different phases depending on the CO coverage: $(\sqrt{3}\times\sqrt{3})$R30° at $\theta_{CO}=0{\cdot}33$, $(2\sqrt{3}\times 2\sqrt{3})$R30° at $\theta_{CO}=0{\cdot}58$, and a compressed phase at the saturation coverage ($\theta_{CO}=0{\cdot}68$). By closely

examining the change of LEED pattern which took place on exposing CO-pre-covered Ru(001) surfaces to NH_3, it was concluded that there were two types of the (2×2) NH_3–CO mixed overlayer having differences in CO/NH_3 ratios; α-(2×2) phase at low CO pre-coverage and the β-(2×2) phase at higher CO pre-coverage.

The amount of dissociated ammonia was determined by means of temperature programmed desorption (TPD) experiments. The results are shown in the inset of figure 15, which shows how the amount of dissociated ammonia varies as a function of CO pre-coverage; it decreases with increasing CO coverage as expected owing to the blocking effect of adsorbed CO, but passes a minimum at $\theta_{CO} \simeq 0{\cdot}25$, increases at higher θ value and reaches a constant value above $\theta_{CO} = 0{\cdot}5$. As described below, the partial coverage of NH_3 decreases from 0·5 for the α-(2×2) phase to 0·25 for the β-(2×2) phase. Thus the above data indicated that the ammonia dissociation was enhanced in the β-(2×2) phase by a factor of four to five as compared with the α-(2×2) phase. The phenomenon was ascribed to the CO-promoted dissociation of NH_3.

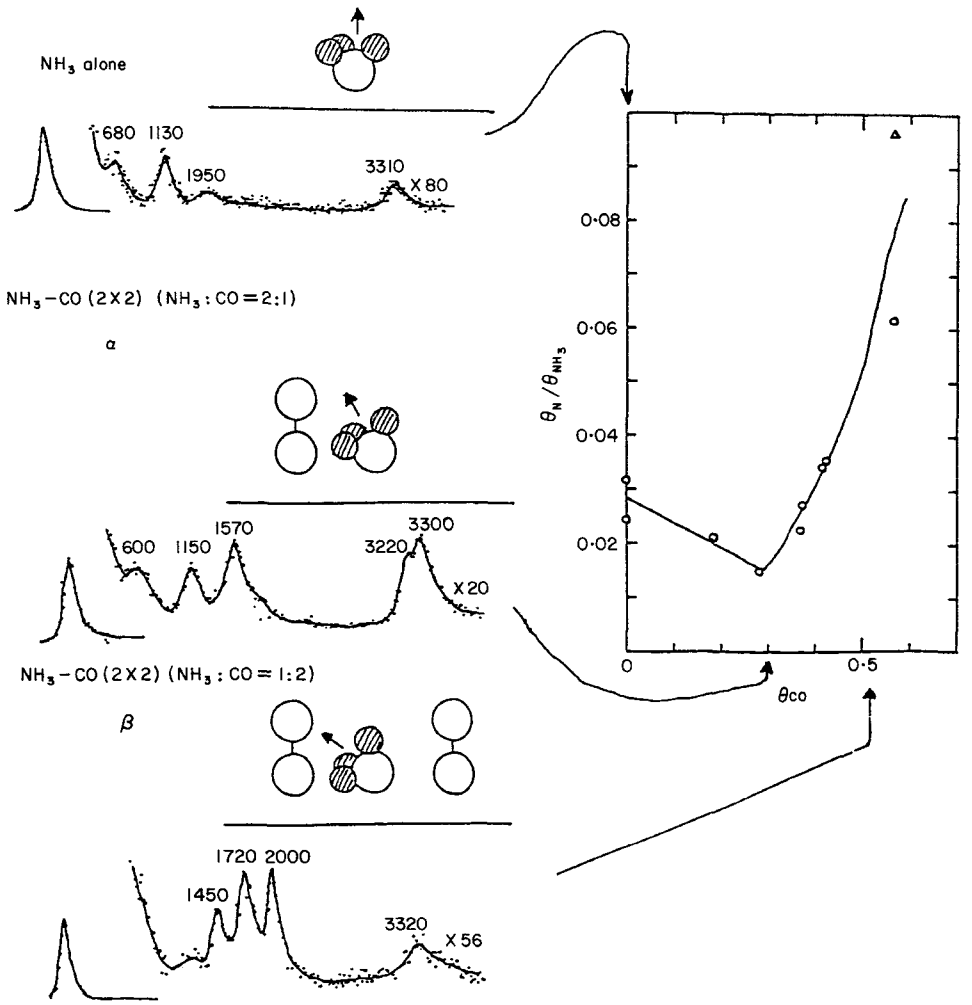

Figure 15. HREEL spectrum of NH_3 R(001) and those of the α- and β-(2×2) phases of the (NH3+CO) mixed overlayer on Rh(001).

HREEL spectra were measured to reveal the surface structures of the (2 × 2) phases and the mechanism of the enhancement of NH_3 dissociation. The spectra obtained at three different states are shown in figure 15. The HREEL spectrum of the $CO(\theta_{CO} \simeq 0{\cdot}3)/Ru(001)$ surface, having (3 × 3)R10° LEED pattern, showed Ru–C and C–O stretching modes at 430 and 2000 cm^{-1} respectively. On exposing this surface to 1·2L $^{15}NH_3$, the C–O stretching peak disappeared and the symmetric and asymmetric deformation peaks of adsorbed ammonia appeared at 1150 and 1570 cm^{-1} as shown in figure 15. The HREEL spectrum of $ND_3/CO(\theta_{CO} \simeq 0{\cdot}3)/Ru(001)$ showed a peak at 1650 cm^{-1} due to the C–O stretching. Thus it was concluded that the C–O stretching peak was shifted downward by the effect of the co-adsorption of NH_3 to overlap on the NH_3 asymmetric deformation peak at 1570 cm^{-1} for the case of the $^{15}NH_3/CO(\theta \simeq 0{\cdot}3)/Ru(001)$ system. Upon heating to 280 K, the peak at 1570 cm^{-1} showed no notable change, but the symmetric deformation peak shifted gradually to 1210 cm^{-1}, while its intensity remained unchanged. The rocking mode decreased drastically in intensity at 200 K and almost disappeared after annealing to 280 K. The N–H stretching mode also decreased intensity upon heating to 200 K, but did not disappear at 280 K. From these results, it was concluded that there were two kinds of ammonia in the α-(2 × 2) phase, the one desorbs at 150–280 K and the other exists on the surface even after heating to 280 K. Upon annealing to 320 K, all the vibrational modes of ammonia disappeared and the C–O stretching peak shifted back to 2000 cm^{-1} in accordance with the LEED observation.

The HREEL spectrum for $^{15}NH_3/CO(\theta_{CO} = 0{\cdot}68)/Ru(001)$ showed three intense loss peaks at 1450, 1720 and 2000 cm^{-1}, and a weak loss feature at 1250 cm^{-1}. Two peaks of 1720 and 2000 cm^{-1} were assigned to the C–O stretching modes of different CO adspecies in the β-(2 × 2) phase. The peaks at 1250 and 1450 cm^{-1} were assigned to the symmetric and asymmetric deformation modes of adsorbed $^{15}NH_3$. After the completion of the α-(2 × 2) phase, no further CO adsorption occurred on the CO exposure at 100 K. Annealing to 300 K, followed by exposure to 6L CO, resulted in the appearance of a C–O stretching peak at 2020 cm^{-1}. The spectrum resembled that of the β-(2 × 2) phase. These results indicated that the weakly adsorbed NH_3 molecule in the α-(2 × 2) phase and one of the CO species in the β-(2 × 2) phase were occupying the same on-top adsorption site. The structures of the two (2 × 2) phases which were concluded on the basis of these observations are shown in figure 16. The α-(2 × 2) phase contains two different ammonia and one CO species per unit mesh, while the β-(2 × 2) phase contains one ammonia and two different CO species per unit mesh.

From the comparison of the intensities of the loss peaks due to the symmetric and asymmetric deformation mode of adsorbed NH_3, it was concluded that the C_{3v} molecular axis of NH_3 was only a little tilted from the surface normal in the α-(2 × 2) phase, but was markedly tilted close to the surface in the β-(2 × 2) phase. As shown in figure 15, the ammonia dissociation is minimum in the α-(2 × 2) phase and is most enhanced in the β-(2 × 2) phase. Thus the CO-promoted ammonia dissociation was considered to be associated with the exhaustive tilting of NH_3 in the β-(2 × 2) structure.

4.3.2. *Alkali-metal overlayers on Cu and Si surfaces*

Aruga *et al.* (1985) constructed an apparatus for observing the change of LEED pattern with time. The LEED pattern is converted into a video signal via a high-sensitivity video camera which employs a silicon-intensifier target tube, and the video signal is recorded in a video-disk recorder which can be externally triggered step-by-step to record signal frames. The time required to record each frame is about 67 ms.

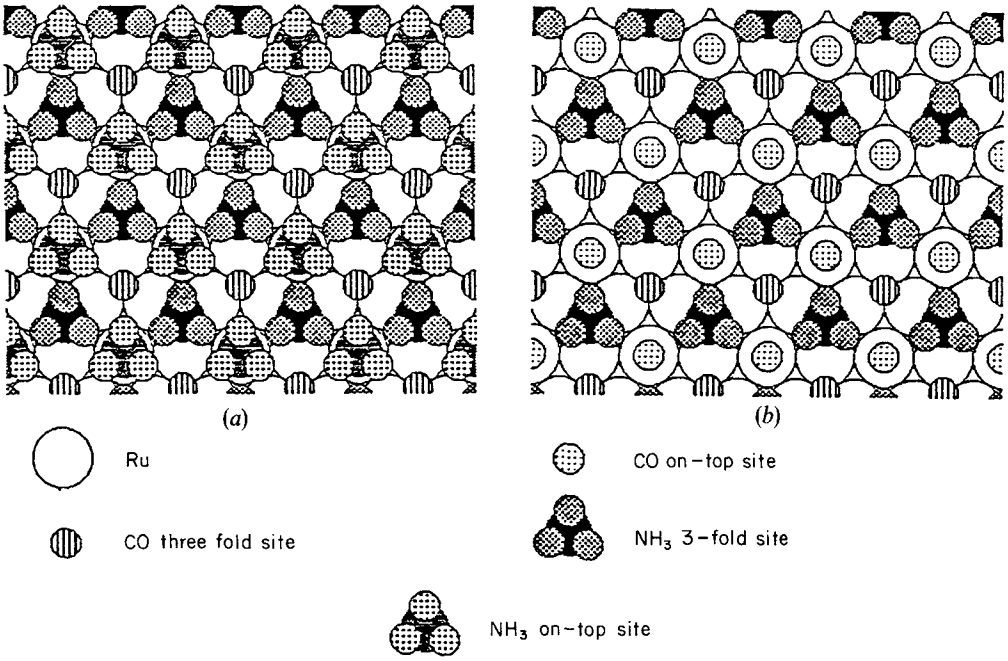

Figure 16. Structures of (*a*) the α- and (*b*) the β-(2 × 2) phases of the NH_3–CO mixed overlayer on Rh(001).

By use of the above apparatus, they carried out a series of investigations on the structural changes of alkali-metal overlayers formed on Cu(001) surface (Aruga *et al.* 1984b, 1985, 1986a, b). The change in LEED pattern with the surface coverage was studied in detail for the K/Cu(001) system. The observed LEED patterns are schematically shown in figure 17 together with the structure corresponding to each LEED pattern (Aruga *et al.* 1985). At a very low coverage, the LEED pattern exhibited a rise of uniform diffuse background (figure 17 (*a*)), indicating a disordered arrangement of K atoms on the surface. At around $\theta = 0{\cdot}18$, the diffuse background began to decrease its intensity and a halo pattern appeared. A detailed investigation was made on the intensity change of this halo pattern as a function of θ (Aruga *et al.* 1986a). It was concluded from this investigation that a two-dimensional condensation of K atoms takes place at $0{\cdot}18 < \theta < 0{\cdot}26$. A long-range ordering appeared at around $\theta = 0{\cdot}28$ (figure 17 (*c*)), corresponding to the quasi-hexagonal structure shown in figure 17 (*h*). When the coverage exceeded 0·3, the above structure was compressed to give another quasi-hexagonal structure (figure 17 (*d*)). The phase change between the above two phases was confirmed to be associated with a continuous contraction of the quasi-hexagonal unit cell. The K monolayer underwent a commensurate–incommensurate transition at $\theta = 0{\cdot}33$ to form a non-registered hexagonal lattice as shown in figure 17 (*j*). The analysis of the observed LEED pattern indicated that the incommensurate phase corresponded to a rotational epitaxy. The orientation angle ϕ between the surface lattice and the monolayer lattice was found to increase from 3·3° to 6·0° with the increase of the coverage up to $\theta = 0{\cdot}37$. There can be four equiprobable domains in the incommensurate phase, which are rotated by $\pm\phi$ from either the [110] or the [110] azimuth of the substrate. The halo pattern observed in the background was attributed to the disordering of K atoms along the boundaries of those domains.

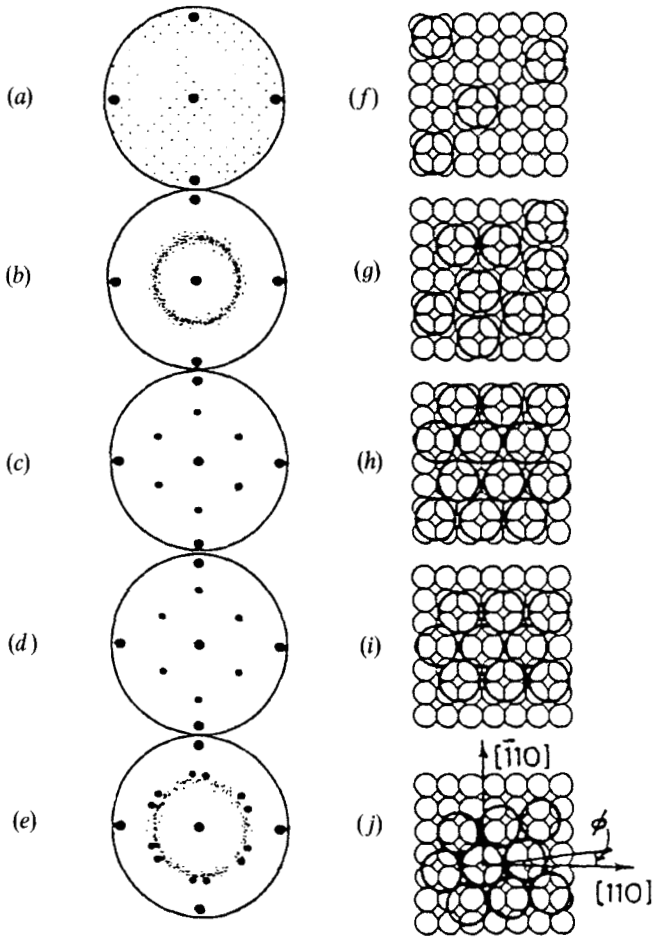

Figure 17. LEED patterns and corresponding structure models of K/Cu(001) for different surface coverage: $\theta < 0{\cdot}18$ (*a*), (*f*); $= 0{\cdot}18$ (*b*), (*g*); $\theta = 0{\cdot}28$ (*c*) (*h*); $0{\cdot}30 < 0 < 0{\cdot}33$ (*d*), (*i*); and $\theta = 0{\cdot}33$ (*e*), (*g*).

Investigation was also done on the alkali-metal overlayers on Si(001)2 × 1 surface by use of electron energy-loss spectroscopy (EELS) (Tochihara and Murata 1982, 1989, Aruga *et al.* 1984a), by synchrotron ultraviolet photoelectron spectroscopy (Tochihara *et al.* 1984) and recently by scanning-tunnelling microscopy (STM) (Hasegawa *et al.* 1989). In alkali metal/Si(001)2 × 1 systems the amount of intermixing between alkali-metal adlayers and silicon substrate is insignificant. This is in great contrast with the case of transition-metal adsorption on Si, where intermixing due to diffusion or silicide formation plays an important role. On the basis of the LEED observation and other experiments, a geometric model shown in figure 18, has been proposed for the alkali-metal atom overlayer on Si(001)2 × 1 at saturation coverage (Levine 1973). According to this model, alkali-metal atoms are arrayed in parallel linear chains along the [110] azimuth of the substrate (see figure 18).

where $|F_o(\mathbf{H})|$ and $|F_c(\mathbf{H})|$ are the observed and calculated structure amplitudes. Most of the refined structures have R values less than 0·070.

Valence electron-density, containing chemically important information, is relatively small compared to the total electron-density in magnitude. Thus a more sensitive function must be introduced to examine the changes undergone in a process of bond formation. One of such functions is the deformation density. This is the difference between the total electron-density and the pro-molecule density, where the pro-molecule density is the electron-density prior to the formation of bonds (i.e. the superposition of spherical free-atom densities each centred at its position in the molecule). The pro-molecule density can be calculated from equations (2) and (3), using spherical atomic scattering factors for f_j.

$$\delta\rho(\mathbf{r}) = \rho(\mathbf{r}) - \rho(\mathbf{r})_{\text{pro-molecule}}. \tag{5}$$

Deformation density represents the rearrangement of the electron-density due to interatomic bonding. Generally the difference between the observed and calculated electron-density is called difference density, which is familiar to X-ray crystallographers.

When atoms form chemical bonds, the valence shell will expand or contract with variation of atomic charge and valence density becomes aspherical. Such behaviour of the valence density can be analysed by least-squares refinement on the basis of observed structure amplitudes. The atomic scattering factor f_j in equation (2) is rewritten as a sum of contributions of core and valence electrons (Dawson 1967, Stewart 1969, Hirshfeld 1977).

$$f_j = f_{j\,\text{core}} + P_{j\,\text{valence}} f_{j\,\text{valence}} + \sum_l \sum_m P_{jlm} f_{jlm}. \tag{6}$$

The second and third terms are the Fourier transforms of the spherical and aspherical valence electron density respectively. $P_{j\,\text{valence}}$ and P_{jlm} are population parameters. The aspherical density fragments in real space are functionally identical to the p, d, f, g... hydrogen atom orbitals, where the angular functions are the well known spherical harmonics, which are labelled with the quantum numbers l and m, with values $l=1$, 2, 3, 4, 5... representing dipolar, quadrupolar, octopolar, hexadecapolar... functions. An important distinction is that this describes the probability distribution of electrons rather than the wavefunctions. A factor multiplying the radial coordinates of the atomic valence density, allowing expansion or contraction of the valence shell with variation of atomic charge is included in the second and third terms in equation (6). By using the expression for f_j given in equation (6) all the adjustable parameters on all atoms can be refined by the least-squares method on the basis of observed structure amplitudes (Hansen and Coppens 1978). This procedure is called multipole refinement. If the aspherical scattering factors obtained after the multipole refinement are used to calculate the electron density, the calculated electron density approaches gradually to the observed density as the refinement proceeds. Thus difference map will eventually becomes featureless, leaving random errors.

3. d-electron-density distribution

Since the aspherical distributions of the 3d electrons in crystals of $[Co(NH_3)_6][Co(CN)_6]$ were detected for the first time (Iwata and Saito 1973), a number of studies on transition metals and their complexes have been carried out (Coppens and Hall 1982, Toriumi and Saito 1983). On the other hand, theoretical

Murata and his collaborators first observed the overlayer-plasmon excitation in the EELS spectra of Cs and K adlayers formed on a Si(001)2 × 1 surface (Tochihara and Murata 1982). They also carried out angle-resolved EELS measurements on the K/Si(001)2 × 2 surface to obtain the overlayer-plasmon dispersion relation (Tochihara *et al.* 1984). EELS spectra were measured by use of a 127° deflector-type electron monochromator and a hemispherical deflector-type electron monochromator and a hemispherical deflector-type analyser. The monochromator was fixed in position, whereas the analyser and sample could be rotated independently about a common latitude axis. The dispersion obtained for the interband-plasmon mode is shown in figure 19, which shows clearly an azimuth-dependent anisotropy. Along the [110] azimuth, the plasmon energy dispersed from 1·7 to 1·95 eV in a small $q_{\|}$ region, whereas along the [100] azimuth the plasmon energy disperses from 1·7 to 1·85 eV in almost the same $q_{\|}$ region. They also observed the intraband-plasmon mode, which was taken as the evidence for the metallic character of the K atom chain formed on the surface. Since the interatomic distance between adjacent K atoms is known to be 3·84 Å along the chain, while the spacing between adjacent chains is 7·68 Å, Murata and his collaborators proposed that the K overlayer has the nature of one-dimensional metal. This finding has attracted strong interest in the surface science community.

EELS experiments were also done on the Li/Si(001)2 × 1 system (Tochihara and Murata 1989). In contrast to the case of other alkali metals, no overlayer-plasmon was observed. In the 2 × 1 structure of the Li overlayer, the interatomic distance along the Li chain, 3·84 Å, is considerably larger than the Li–Li distance in the bulk Li metal. It was concluded that Li atoms form rather strong covalent bonds with Si, like H atoms.

Interesting results were recently reported from scanning tunnelling microscopy (STM) observation on Li and K absorptions on a Si(001)2 × 1 surface (Hasegawa *et al.* 1989). This observation revealed that, at the initial stage of Li (or K) adsorption, alkali atoms are adsorbed at the sites above one of the dimer-forming surface Si atoms and stabilize buckled dimerization. It was also found that adsorbed alkali atoms form linear chains perpendicular to the substrate 2 × 1 dimer rows. These observations are significantly different from the structural model which has been proposed on the bases of LEED and other experiments.

References

ARUGA, T., TOCHIHARA, H., and MURATA, Y., 1984a, *Phys. Rev. Lett.*, **53**, 372; 1984b, *Ibid.*, **52**, 1794; 1985, *Surf. Sci.*, **158**, 490; 1986a, *Ibid.*, 175, L725; 1986b, *Phys. Rev.* B, **34**, 8237.

ASAKURA, K., IWASAWA, Y., and KURODA, H., 1986a, *J. chem. Soc. Japan*, 1539; 1986b, *Bull. chem. Soc. Japan*, **59**, 647.

ASAKURA, K., KITAMURA-BANDO, K., ISOBE, K., SUGI, Y., ARAKAWA, H., and IWASAWA, Y., 1989, (to be published).

ASAKURA, K., YAMADA, M., IWASAWA, Y., and KURODA, H., 1985, *Chem. Lett.*, 511.

BEDZYK, M., and MATERLIK, G., 1985, *Surf. Sci.*, **152/153**, 10.

EDMONDS, T., MCCARROLL, J. J., and PITKETHLY, R. C., 1971, *J. vac. Sci. Tech.*, **8**, 68.

FUNABASHI, M., KITAJIMA, Y., YOKOYAMA, T., OHTA, T., and KURODA, H., 1989b, *Physica* B, **158**, 666.

FUNABASHI, M., OHTA, T., YOKOYAMI, T., KITAJIMA, Y., and KURODA, H., 1989a, *Rev. scient. Instrum. nucl. Instrum.*, **60**, 2505.

GOLVOCHENKO, J. A., BATTERMAN, B. W., and BROWN, W. L., 1974, *Phys. Rev.* B, **10**, 4239.

GOLVOCHENKO, J. A., PATEL, J. R., KAPLAN, D. R., COWAN, P. L., and BEDZYK, M. J., 1982, *Phys. Rev. Lett.*, **49**, 560.

HASEGAWA, Y., HASHIZUME, T., KAMIYA, I., IDE, T., SUMITA, I., HYODO, S., SAKURAI, T., TOCHIHARA, H., KUBOTA, M., and MURAMATA, Y., 1989, *Tech. Rep. Inst. Solid St. Phys., Univ. Tokyo*, Ser. A, No. 2147.

ICHIKAWA, M., 1978, *Bull. chem. Soc. Japan.*, **51,** 2168, 2173; 1979, *J. Catal.*, **59,** 67.
IIJIMA, S., and ICHIKAWA, M., 1985, *J. Catal.*, **94,** 313.
IWASAWA, Y., 1985, *Tailored Metal Catalysts*, edited by Y. Iwasawa (Dordrecht: Reidel), p. 58; 1989, *Catal. Today* (to be published).
IWASAWA, Y., ASAKURA, K., ISHII, H., and KURODA, H., 1986, *Z. phys. Chem.* Neue Folge., **144,** 105.
IWASAWA, Y., ITO, N., CHIBA, T., ISHII, H., and KURODA, H., 1985a, *Chem. Lett.*, 1141.
IWASAWA, Y., ITO, N., ISHII, H., and KURODA, H., 1985b, *J. chem. Soc. chem. Commun.*, 827.
IWASAWA, Y., SATO, Y., and KURODA, H., 1983a, *J. Catal.*, **82,** 289.
IWASAWA, Y., and TANAKA, H., 1984, *Proceedings of the Eighth International Congress on Catalysis*, 1984, IV-381.
IWASAWA, Y., YAMADA, M., OGASAWARA, S., SATO, Y., and KURODA, H., 1983b, *Chem. Lett.*, 621.
IWASAWA, Y., YAMADA, M., SATO, Y., and KURODA, H., 1984, *J. molec. Catal.*, **23,** 95.
IWASAWA, Y., and YAMAGISHI, 1983, *J. Catal.*, **82,** 373.
LEVINE, J. K., 1973, *Surf. Sci.*, **34,** 901.
KITAJIMA, Y., KOSUGI, N., KURODA, H., and OHTA, T., 1986, *J. chem. Soc. Japan*, 1547.
KITAJIMA, Y., YOKOYAMA, T., FUNABASHI, M., OHTA, T., and KURODA, H., 1989, *Physica* B, **158,** 668.
KITAMURA-BANDO, K., ISOBE, K., SUGI, Y., ASAKURA, H., and IWASAWA, Y., 1989, *J. chem. Soc. chem. Commun.* (to be published).
MATERLIK, G., FRAHM, A., and BEDZYK, M. J., 1984, *Phys. Rev. Lett.*, **52,** 441.
MATERLIK, G., and ZEGENHAGEN, J., 1984, *Phys. Lett.* A, **104,** 47.
NAMBA, H., and KURODA, H., 1986, RCS Report, No. 4.
NAMBA, H., DAIMON, H., IDEI, Y., KOSUGI, N., KURODA, H., TANIGUCHI, M., SUGA, S., MURATA, Y., UEYAMA, K., and MIYAHARA, T., 1989, *Rev. Scient. Instrum.*, **60,** 1909.
OHTA, T., KITAJIMA, Y., KURODA, H., TAKAHASHI, T., and KIKUTA, S., 1986b, *Nucl. Instrum. Meth.* A, **246,** 760.
OHTA, T., KITAJIMA, Y., STEFAN, P. M., STEFAN, M. S., KOSUGI, N., and KURODA, H., 1986c, *J. Phys., Paris*, **47,** C8–503.
OHTA, T., SEKIYAMA, H., KITAJIMA, Y., KURODA, H., TAKAHASHI, T., and KIKUTA, S., 1985, *Japan J. appl. Phys.*, **24,** L475.
OHTA, T., STEFAN, P. M., NOMURA, M., and SEKIYAMA, Y., 1986a, *Nucl. Instrum. Meth.* A, **246,** 373.
OYANAGI, H., MATSUSHITA, T., ITO, M., and KURODA, H., 1984, KEK Report 83–30 (Research Center for Spectro-chemistry, University of Tokyo).
SASAKI, T., ARUGA, T., KURODA, H., and IWASAWA, Y., 1989, *Surf. Sci. Lett.* (to be published).
SATO, Y., IWASAWA, Y., and KURODA, H., 1982, *Chem. Lett.*, 1101.
SATOW, Y., ASAKURA, K., and KURODA, H., 1987, *J. Phys.* C, **20,** 5027.
TAKATA, Y., YOKOYAMA, T., OHTA, T., KITAJIMA, Y., FUNABASHI, M., and KURODA, H., 1989, (to be published).
TOCHIHARA, H., KUBOTA, M., ARUGA, T., MIYANO, M., and MURATA, Y., 1984, *Japan J. appl. Phys.*, **23,** L271.
TOCHIHARA, H., and MURATA, Y., 1982, *J. phys. Soc. Japan*, **51,** 2920; 1989, *Surf. Sci.*, **215,** L323.
TOHJI, K., and UDAGAWA, Y., 1984, *Jap. J. appl. Phys.*, **89,** 5671.
TOHJI, K., UDAGAWA, Y., MIZUSHIME, T., and UENO, A., 1985, **89,** 5671.
YOKOYAMA, T., YAMAZAKI, K., KOSUGI, N., KURODA, H., ICHIKAWA, M., and FUKUSHIMA, T., 1984, *J. chem. Soc. chem. Commun.*, 962.
YOKOYAMA, T., ASAKURA, K., IWASAWA, Y., and KURODA, H., 1986, *J. Phys., Paris*, **47,** C8–273; 1989c, *J. phys. Chem.*, **93,** 1023.
YOKOYAMA, T., KIMOTO, S., and OHTA, T., 1989a, *Jap. J. appl. Phys.*, **28,** L851; 1989b, *Physica* B, **158,** 255.
YOKOYAMA, T., TAKATA, Y., YOSHIKI, M., OHTA, T., FUNABASHI, M., KITAJIMA, Y., and KURODA, H., 1989d, *Jap. J. appl. Phys.*, **28,** L1637.
YOKOYAMA, T., FUNABASHI, M., KITAJIMA, Y., OHTA, T., and KURODA, H., 1989e, *Physica* B, **158,** 643.